

OPTIKS: Optimized Gradient Properties Through Timing in K-Space

Matthew A. McCready, Xiaozhi Cao, Kawin Setsompop, John M. Pauly, and Adam B. Kerr

Abstract—A customizable method (OPTIKS) for designing fast trajectory-constrained gradient waveforms with optimized time domain properties was developed. Given a specified multidimensional k -space trajectory, the method optimizes traversal speed (and therefore timing) with position along the trajectory. OPTIKS facilitates optimization of objectives dependent on the time domain gradient waveform and the arc-length domain k -space speed. OPTIKS is applied to design waveforms which limit peripheral nerve stimulation (PNS), minimize mechanical resonance excitation, and reduce acoustic noise. A variety of trajectory examples are presented including spirals, circular echo-planar-imaging, and rosettes. Design performance is evaluated based on duration, standardized PNS models, field measurements, gradient coil back-EMF measurements, and calibrated acoustic measurements. We show reductions in back-EMF of up to 94% and field oscillations up to 91.1%, acoustic noise decreases of up to 9.22 dB, and with efficient use of PNS models speed increases of up to 11.4%. The design method implementation is made available as an open source Python package through GitHub.

Index Terms—Gradient waveform design, Magnetic resonance imaging (MRI), Optimal control, k -space trajectories, Safety

I. INTRODUCTION

HIGH performance gradient hardware has seen growing popularity in recent years, in order to facilitate fast high-resolution MRI [1], [2]. Demand for fast imaging, and improvements in image reconstruction have also led to a wide range of non-Cartesian k -space sampling trajectories [3]–[7]. With increased gradient amplitudes, faster slew-rates, and asymmetric coil designs comes greater risk to patient and system safety.

Prolonged exposure to rapidly varying magnetic fields can cause patients to experience peripheral nerve stimulation (PNS), a major source of discomfort in rapid imaging. Limits on PNS threshold are imposed by an international engineering standard (IEC 60601-2-33) [8] and apply to every scan of a human with an MRI. The maximum PNS limit (P_{max}) often

prevents operating the gradient system at its maximum slew-rate (S_{max}) and by extension maximum gradient amplitude (G_{max}).

Gradient waveforms are often globally de-rated to a slew-rate much less than S_{max} to meet PNS limits thus resulting in longer scan times. Previous work has optimized fast PNS approved spirals by introducing a P_{max} -limited region in addition to existing G_{max} and S_{max} -limited regions [9]. Faster EPI sequences have also met P_{max} by empirically replacing ramp periods with \tanh functions [9]. Methods have also been presented for optimization of k -space trajectory constrained by P_{max} , but these cannot follow a pre-specified trajectory and are designed for a user-chosen readout time with no option for time optimization [7].

Rapid variation of gradient fields is also the source of gradient coil vibration. Playing out a gradient waveform modulates the magnitude and direction of current flow in the coils and therefore the Lorentz forces they experience. This drives vibrations and deformations of the coils in tandem with the gradient waveform. In particular, if a gradient waveform contains power at the mechanical resonance frequencies of the coils it will excite those resonances, producing strong and long lasting vibrations. This can result in permanent damage to the coils and produce oscillatory error fields [1], [2]. Furthermore, eddy currents induced on conducting surfaces in the scanner by the gradients will experience these vibrations. Components close to the liquid helium bath, such as the radiation shield, can deposit large amounts of energy into the helium causing it to boil off when vibrated [2], [10]. This loss of helium is expensive to replace and can put the system in danger of quenching posing a major safety risk to both system and patient. Limited methods have been presented for producing compact spectrum spiral waveforms [11], and frequency controlled waveforms with fixed timing and a set zeroth moment [12]. A heuristic method has been developed for reducing waveform power in specified bands based on control of an assumed instantaneous frequency [13], but does not take into account transient effects and in some cases *increases* mechanical resonance vibrations. Currently there is no method for explicit gradient frequency control while following a specified trajectory.

Gradient waveform driven vibrations are also responsible for loud acoustic noise present in MRI exams. This is the number one source of patient discomfort and had been the focus of many studies to make sequences quieter. Current methods to design quiet gradient waveforms severely band-limit the waveforms [14], [15]. These methods are highly restricted in applicable trajectories, and lack finer frequency control to cancel out loud vibration bands below the set band-

This work was supported in part by the National Institutes of Health (NIH) under Grant R01 EB009690, and Grant U01 EB029427, as well as funding from the Natural Sciences and Engineering Research Council of Canada (NSERC) PGS-D and GE Healthcare.

M. A. McCready is with the Department of Electrical Engineering and the Stanford Center for Cognitive and Neurobiological Imaging, Stanford University, Stanford, CA 94305 USA (e-mail: mattmc@stanford.edu).

X. Cao is with the Department of Radiology, Stanford University, Stanford, CA 94305 USA (e-mail: xiaozhic@stanford.edu).

K. Setsompop is with the Department of Radiology, Stanford University, Stanford, CA 94305 USA (e-mail: kawins@stanford.edu).

J. M. Pauly, is with the Department of Electrical Engineering, Stanford University, Stanford, CA 94305 USA (e-mail: pauly@stanford.edu).

A. B. Kerr is with the Department of Electrical Engineering and the Stanford Center for Cognitive and Neurobiological Imaging, Stanford University, Stanford, CA, 94305 USA (e-mail: akerr@stanford.edu).

limit. Scanner specific acoustic transfer functions (ATFs) have been measured under a linear-time-invariant assumption to predict acoustic noise based on the input gradient waveform [16], [17]. A method for gradient frequency control could use ATFs to efficiently reduce acoustic noise while following specified readout trajectories.

A time-optimal method for gradient waveforms which follow arbitrary trajectories is developed in [18]. A framework is presented where gradient waveforms are designed by optimizing speed for following an arbitrary k -space trajectory, as a function of distance along the curve (arc-length). This is used to find waveforms which trace out k -space trajectories in minimum time adhering to G_{max} and S_{max} , an optimal control problem with an explicit solution. While efficient, the method is highly inflexible with regard to inclusion of time-domain waveform properties.

In this work we present a method to design gradient waveforms with optimized properties by modifying timing in k -space (OPTIKS) for any prescribed trajectory. We expand upon the k -space speed approach developed in [18] by replacing the explicit time-optimal solution with an iterative gradient descent optimization. This method allows the optimization of k -space speed as a function of trajectory arc-length $v(s)$ that minimizes a loss function $L(v(s), g(t\{v(s)\}))$, bridging the gap between time-domain waveform optimization objectives and the optimal arc-length domain speed. We then apply this new method to design fast gradient waveforms which adhere to G_{max} and S_{max} , while for the first time allowing for PNS, and frequency control without trajectory deviation. The method is made available as an open source Python package through GitHub (<https://github.com/mattmc-stanford/optiks>).

II. METHODS

Solving for $v(s)$ determines timings for passing through each point along the k -space curve $C(s)$ [18]. With timings determined, $g(t)$ is directly calculated via time differentiation of $C(t)$. Lustig et al explicitly solve (1) [18] for the $v(s)$ which minimizes waveform duration T with constraints on $v(s)$ and its derivative as a function of arc-length. These constraints enforce the limits on gradient amplitude and slew-rate in the arc-length domain and incorporate the length L trajectory geometry through its curvature $\kappa(s)$

$$\begin{aligned} \min_{v(s)} \quad & \int_0^L ds/v(s) \\ \text{subject to} \quad & v(s) \leq \min \left\{ \gamma G_{max}, \sqrt{\gamma S_{max}/\kappa(s)} \right\} \\ & |v'(s)| \leq \frac{1}{v(s)} \sqrt{\gamma^2 S_{max}^2 - \kappa(s)^2 v(s)^4} \\ & v(0) = 0. \end{aligned} \quad (1)$$

The problem we seek to solve here is rooted in the same optimization – optimizing speed for arbitrary trajectories – but with the goal of optimizing some time domain property of the resulting gradient waveform. The problems presented here do not have explicit solutions and will be solved using back-propagation with the iterative gradient descent optimizer “Adam” included in PyTorch.

A. Differentiable Domain Transformations

Extending the optimization problem to time domain waveform properties requires a differentiable conversion from $v(s)$ to $g(t)$. The forward pass consists of calculating timing as a function of arc-length through $t(s) = \int_0^s d\sigma/v(\sigma)$, then interpolating the initial arbitrarily parameterized discrete trajectory to be evenly sampled in time. Once $C(t)$ is acquired, $g(t)$ can be calculated by differentiation of the trajectory with respect to time.

Interpolation presents an issue for back-propagation as the binning and resampling operation applied to the independent variables is not differentiable. The gradient is approximated then by assuming the operation is performed by a pair of constant copying matrices with no dependence on the optimization variables. The full backward pass through interpolation is given in greater detail in Appendix A.

B. Time Domain Constraint Enforcement

Some waveform properties have a single limiting value which must be enforced as a constraint rather than general optimization. For example, waveforms are often limited by P_{max} or S_{max} , or there may be some maximum duration we are willing to allow the waveform. Despite the non-convex nature of the problem presented here, we will apply a common approach to constraints used in convex problems. We introduce the log-barrier function (2) which takes the loss asymptotically to infinity as input x approaches its maximum allowed value x_{max}

$$\text{logb}(x, x_{max}) = - \sum_x \ln(x_{max} - x). \quad (2)$$

While the log-barrier is convex in $v(s)$ when setting a maximum duration, for time domain properties the use of a log-barrier presents an issue. Optimization in the arc-length domain while carried out in small steps can easily propagate to larger changes in $g(t)$ properties which violate a log-barrier. This would result in infinite loss and halt the gradient descent process. To remedy this we introduce a “leaky” log-barrier function defined in (3)

$$\text{logb}^*(x, x_{max}, \delta) = \begin{cases} \text{logb}(x, x_{max}) & x \leq x_\delta \\ \sum_x \frac{x-x_\delta}{\delta} - \log(\delta) & \text{otherwise.} \end{cases} \quad (3)$$

The leaky log-barrier function becomes linear beyond some point $x_\delta = x_{max} - \delta$ with continuous first derivative. The choice of δ determines the slope of the linear region, and therefore how hard the gradient descent is pushed back below the limit x_{max} (Fig. 1).

C. Time Optimal Gradient Descent

We now have the tools to translate the minimum time problem (1) into a form suitable for gradient descent. Enforcing the speed and speed-derivative constraints is necessary for designing feasible waveforms. The first constraint or “speed limit” can be enforced directly by introducing a placeholder variable $\xi(s)$, defined by (4)

$$v(s) \equiv \min \left\{ \gamma G_{max}, \sqrt{\gamma S_{max}/\kappa(s)} \right\} \cdot \sigma(\xi(s)). \quad (4)$$

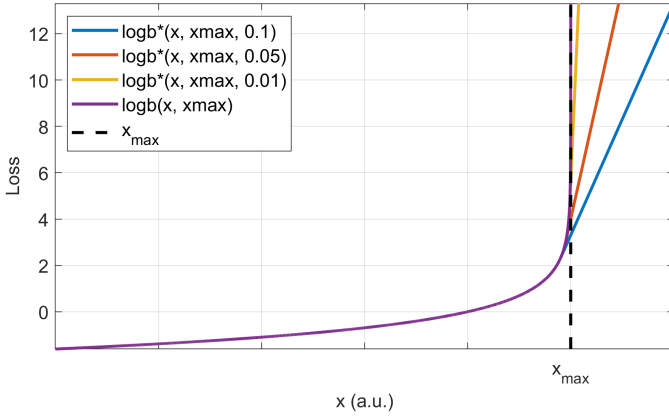


Fig. 1. Comparison of log-barrier function (purple) to leaky log-barriers with varying relaxations. Smaller δ values result in steeper slopes beyond x_{max} .

Rather than optimizing $v(s)$ we optimize $\xi(s)$ and transform through (4) where σ is the sigmoid function. This smoothly scales $v(s)$ to be between its lower bound 0 and the upper bound from (1), eliminating the speed limit constraint. However, the speed *derivative* constraint forms a nonlinear differential inequality and cannot be directly enforced. The speed derivative constraint only relates to the S_{max} limit and can be replaced with a leaky log-barrier loss term applied to slew-rate in the time domain. The result for the time-optimal gradient descent problem is given in (5) where δ_S is the switching proximity to S_{max} and λ_1 and λ_2 are relative weightings for the time minimization and slew-rate constraints respectively

$$\begin{aligned} \min_{\xi(s)} \quad & \lambda_1 \int_0^L ds/v(s) + \lambda_2 \log b^*(\|\mathbf{S}(t)\|_2, S_{max}, \delta_S) \\ \text{s. t.} \quad & v(s) \equiv \min \left\{ \gamma G_{max}, \sqrt{\gamma S_{max}/\kappa(s)} \right\} \cdot \sigma(\xi(s)). \end{aligned} \quad (5)$$

D. Peripheral Nerve Stimulation Control

PNS is often more limiting in waveform design than system limits. We can impose a PNS limit P_{max} on our waveforms by including an additional leaky log-barrier term in the optimization. In this work we use the standard PNS calculation set by the international electromechanical commission (IEC) as convolution of slew-rate with a nerve response function in (6) [8]

$$\begin{aligned} h(t) &\equiv \frac{\alpha c}{r(c+t)^2} \quad \forall t \geq 0 \\ P(t) &= 100 \|h(t) * \mathbf{S}(t)\|_2. \end{aligned} \quad (6)$$

The nerve response $h(t)$ is determined by system hardware, with rheobase r , chronaxie time c , and effective coil length α gradient coil specific constants provided by manufacturers. Note that any PNS calculation which is differentiable with respect to $\mathbf{g}(t)$ could be used in place of (6) (e.g. the ‘‘SAFE’’ model [19]). Incorporating the PNS threshold limit into the

optimization gives (7)

$$\begin{aligned} \min_{\xi(s)} \quad & \lambda_1 \int_0^L ds/v(s) + \lambda_2 \log b^*(\|\mathbf{S}(t)\|_2, S_{max}, \delta_S) \\ & + \lambda_3 \log b^*(P(t), P_{max}, \delta_P) \\ \text{s. t.} \quad & v(s) \equiv \min \left\{ \gamma G_{max}, \sqrt{\gamma S_{max}/\kappa(s)} \right\} \cdot \sigma(\xi(s)). \end{aligned} \quad (7)$$

E. Mechanical Resonance Control

Vibration controls can only be implemented by passing through the time domain. The simplest design method for avoiding mechanical resonance is to identify the set of resonance frequency bands \mathcal{M} and minimize power deposition within them as a term of the loss function (8)

$$\begin{aligned} \min_{\xi(s)} \quad & \lambda_1 \int_0^L ds/v(s) + \lambda_2 \log b^*(\|\mathbf{S}(t)\|_2, S_{max}, \delta_S) \\ & + \lambda_3 \|\mathcal{F}\{\mathbf{g}(t)\}|_{f \in \mathcal{M}}\|_2^2 \\ \text{s. t.} \quad & v(s) \equiv \min \left\{ \gamma G_{max}, \sqrt{\gamma S_{max}/\kappa(s)} \right\} \cdot \sigma(\xi(s)). \end{aligned} \quad (8)$$

Another option is to directly limit the predicted oscillation either of field or physical displacement caused by the waveform. This requires the measurement of a vibration based impulse response function.

F. Acoustic Noise Reduction

Acoustic noise reduction is an extension of the mechanical resonance control problem. With a system-specific ATF the acoustic noise generated by a sequence can be predicted directly from the gradient waveforms. By including the predicted acoustic noise power as a term of the loss function we can design quieter waveforms (9)

$$\begin{aligned} \min_{\xi(s)} \quad & \lambda_1 \int_0^L ds/v(s) + \lambda_2 \log b^*(\|\mathbf{S}(t)\|_2, S_{max}, \delta_S) \\ & + \lambda_3 \|\mathbf{A}(f) \mathcal{F}\{\mathbf{g}(t)\}\|_2^2 \\ \text{s. t.} \quad & v(s) \equiv \min \left\{ \gamma G_{max}, \sqrt{\gamma S_{max}/\kappa(s)} \right\} \cdot \sigma(\xi(s)). \end{aligned} \quad (9)$$

Where $\mathbf{A}(f)$ is the ATF in the frequency domain. Minimizing acoustic power in the frequency domain is equivalent to minimizing power in the predicted acoustic waveform by Parseval’s Theorem.

G. Resonance Characterization

To avoid vibrations at mechanical resonances, the resonance frequency bands were identified. Each gradient axis was probed by playing 120 ms duration sinusoids at every 10Hz from 50-2000 Hz and collecting field or back-EMF measurements for 20 ms following each waveform. Oscillatory error fields produced by lingering vibrations were monitored using a dynamic field camera (Skoep, Zurich, Switzerland). The back-EMF produced by motion of the coils through the main magnetic field was also monitored using a digital scope (ADP3450, Diligent, Pullman, WA, USA) connected to the bridge voltage of the current controlled gradient power amplifier.

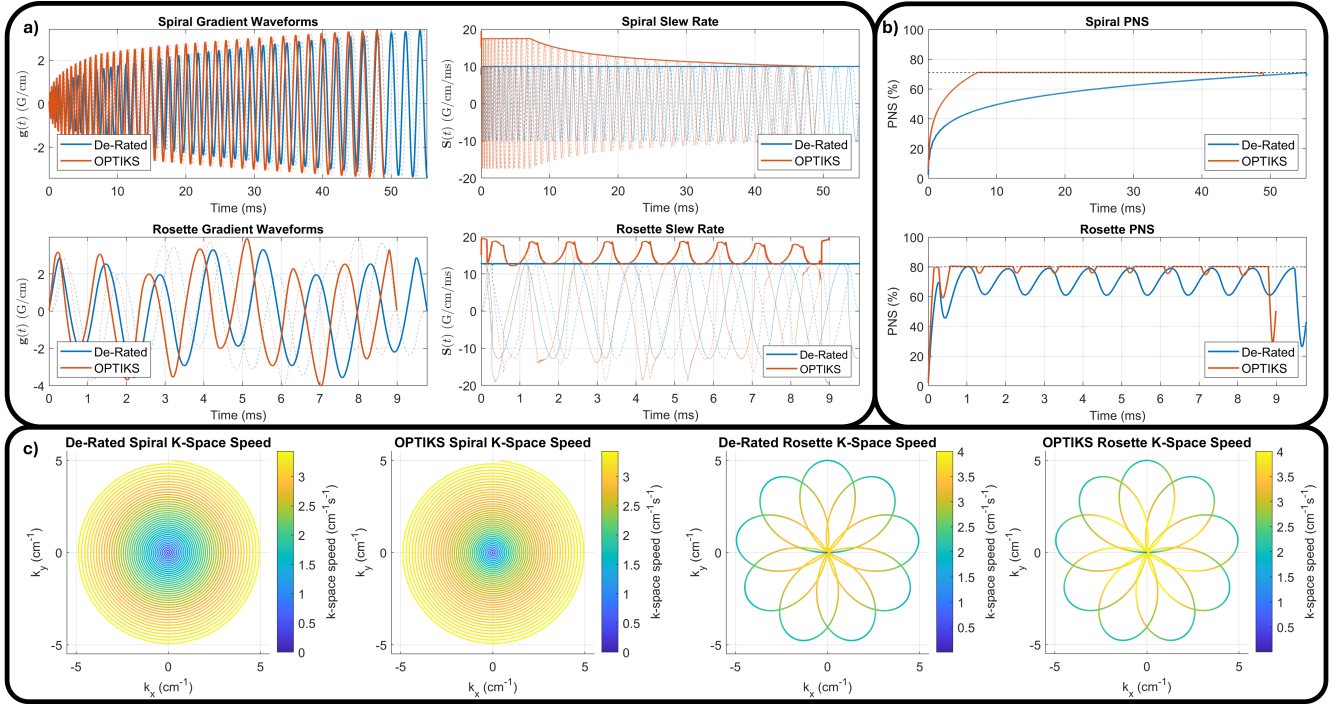


Fig. 2. OPTIKS PNS-limited spiral and rosette designs for UHP. **a)** Gradient waveforms for time-optimal (blue) and PNS-limited (orange) spiral and rosette (dashed Y channel). Slew-rate for the waveforms, dark solid lines indicate magnitude across X and Y channels, faint solid and dashed lines indicate X and Y axes respectively. **b)** PNS response for waveforms from a) with dashed black line indicating P_{max} . **c)** Resulting k -space trajectories with color indicating speed along curve at each point.

In both cases the measured oscillatory signals were represented by their RMS values at each input frequency to produce a spectrum of vibration intensity. Peaks in these spectra appear at the resonance bands and can be avoided in the gradient waveform design using (8).

H. Acoustic Characterization

ATFs were measured in-house for the GE 3T UHP and PREMIER systems to design OPTIKS waveforms with reduced acoustic noise. A pair of MR safe noise canceling headphones (OptoActive III, Optoacoustics Ltd., Mazor, Israel) with built-in calibrated microphones were placed 20 cm apart centered at isocenter on the patient table with the ear side facing up. The sound pressure level (SPL) was recorded during characterization waveforms played on each gradient axis. The audio output was connected to an Analog Discovery Pro for digitization. Sinusoids spaced every 10 Hz from 200-3130 Hz were each played and recorded for a duration of 160 ms. A reference waveform of 1000 Hz was recorded for each axis for a duration of 1 s.

The ATF for each system was fit using a least-squares solution of Fourier transformed input gradient waveforms $I_j(f)$ and output acoustic measurements $O_j(f)$ (10)

$$H_i(f) = \frac{\sum_j I_{i,j}^*(f) \cdot O_{i,j}(f)}{\sum_j |I_{i,j}(f)|^2} \quad \forall i = x, y, z. \quad (10)$$

And scaled to match the reference measurement at 1000 Hz.

III. RESULTS

In this section, we present examples of OPTIKS waveforms designed to limit PNS, minimize mechanical resonances, and reduce acoustic noise. We evaluate these designs based on theoretical PNS models, field camera measurements, back-EMF measurements, and acoustic measurements, and confirm that image quality is maintained with OPTIKS waveforms.

A. Peripheral Nerve Stimulation Limited Waveforms

PNS-limited waveforms were designed using OPTIKS for the GE 3T UHP system. Two examples were considered; a 1 mm isotropic resolution 22 cm FOV variable density spiral and a 1 mm nine-petal rosette (Fig. 2). The waveforms were designed with $S_{max} = 19.5$ G/cm/ms and $G_{max} = 10$ G/cm. The spiral was prescribed a P_{max} of 72% while the rosette was prescribed 80%. The design functional consisted of time minimization, slew-rate limiting, and PNS limiting terms (7).

The OPTIKS waveforms were compared to time-optimal waveforms designed using (1) with globally derated S_{max} to meet the target P_{max} values. For these specific trajectories and PNS limits the OPTIKS spiral requires a traversal time 6.31 ms shorter than its time-optimal counterpart, while the OPTIKS rosette is shorter by 0.79 ms. These equate to 11.4% and 8.1% reductions in traversal time respectively.

B. Mechanical Resonances and Safe Waveforms

Mechanical resonance excitation is particularly prominent in trajectories with periodic oscillations. Spiral and circular echo-planar-imaging (CEPI) trajectories have gradient waveforms

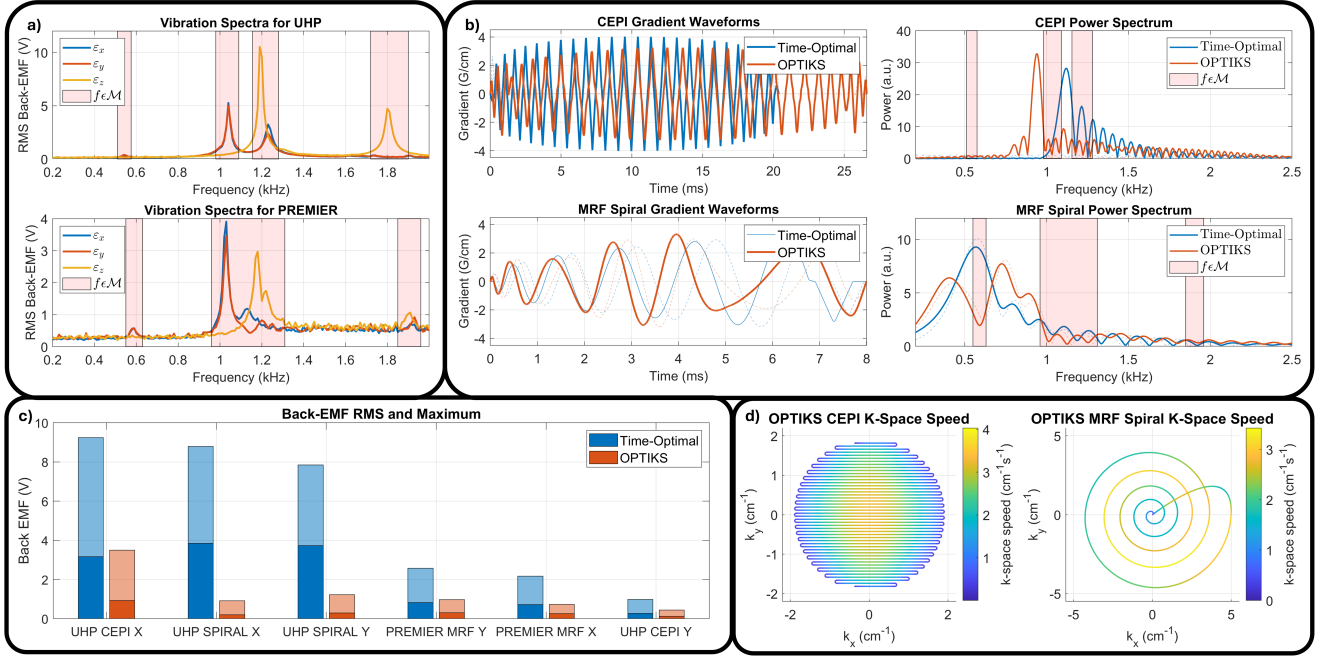


Fig. 3. Mechanical resonance measurements and designs for UHP and PREMIER systems. **a)** Vibration spectra calculated from RMS back-EMF for UHP and PREMIER gradient systems. Mechanical resonances highlighted in red. **b)** Gradient waveforms for time-optimal (blue) and OPTIKS mechanical resonance-optimized (orange) CEPI on UHP and MRF spiral on PREMIER, along with their power spectra. Solid and dashed lines representing X- and Y-axis data respectively. **c)** RMS and maximum value of back-EMF measured from time-optimal test waveforms and OPTIKS waveforms on UHP and PREMIER systems. Darker shorter bar gives RMS value, taller lighter bar gives maximum value. **d)** Resulting k -space trajectories with color indicating speed along curve at each point for OPTIKS waveforms from **b)**.

which sweep through a large range of frequencies, exciting multiple mechanical resonances. OPTIKS was employed to minimize mechanical resonance excitations from a CEPI waveform and single-shot spiral for the GE 3T UHP system, and a variable density magnetic resonance fingerprinting (MRF) spiral for the GE 3T PREMIER system [20], [21]. All waveforms were compared to their time-optimal counterparts (Fig. 3).

The CEPI trajectory was chosen to be 2.8 mm isotropic resolution with a 26 cm FOV and $R_y = 2$. These trajectory parameters result in gradient waveforms with power centered at the mechanical resonance bands in the time-optimal solution. The UHP spiral was designed with a 2 mm isotropic resolution and 24 cm FOV. All UHP waveforms were designed with $S_{max} = 20$ G/cm/ms and $G_{max} = 10$ G/cm. The OPTIKS designed CEPI waveforms reduced the RMS back-EMF by 70.8% on the readout axis (X) and 55.2% on the phase encode axis (Y), while the RMS oscillatory field was reduced by 56.3% and 51.7% respectively. The OPTIKS designed spiral waveforms reduced the RMS back-EMF by 94.8% and the RMS oscillatory field by 91.1%. These improvements came at the expense of speed with a 30% and 15% increase in duration respectively.

The spiral trajectory used for MRF in the PREMIER system was designed with a 1 mm isotropic resolution and a 22 cm FOV. A variable-density spiral design was employed, with the undersampling factor increasing linearly from $R = 16$ at the k -space center to $R = 32$ at the end of the spiral interleaf, enabling faster acquisition. To ensure that the TR

remained constant and thus preserve the consistency of the MRF dictionary, the OPTIKS spiral waveform was designed to match the duration of the original time-optimal waveform. To offset the cost of mechanical resonance minimization, S_{max} was increased from 10 G/cm/ms to 15 G/cm/ms and a PNS limit term (7) was included in the design with $P_{max} = 80\%$. The OPTIKS designed MRF spiral reduced the RMS back-EMF by 63.8%. A field camera was not available for measurements on the PREMIER. Reconstructed T1 and T2 maps from the MRF sequence are shown for the time-optimal and OPTIKS designed spiral acquisitions in Fig. 5. Both images were acquired with informed consent from the subject.

Mechanical resonance spectra obtained by back-EMF measurement for the UHP and PREMIER systems, and by field camera measurement for the UHP system are given in Fig. 3 and Fig. 4 respectively. Targeted mechanical resonance bands \mathcal{M} are highlighted in red.

C. Acoustic Characterization and Quieter Spirals

The ATF for the PREMIER and UHP systems are given in Fig. 6. Measurements are positionally dependant and the ATF for each gradient axis was made up of the maximum measured values at each frequency for ATFs fit from two headphones. A $R = 3$ rewind spiral with 2 mm isotropic resolution and 22 cm FOV was used for an acoustic minimization experiment on the PREMIER system. Three waveforms were designed for the spiral. A 16.628 ms time-optimal waveform and an OPTIKS waveform of 20.6 ms duration were designed with $S_{max} = 13.5$ G/cm/ms. A waveform of equal duration

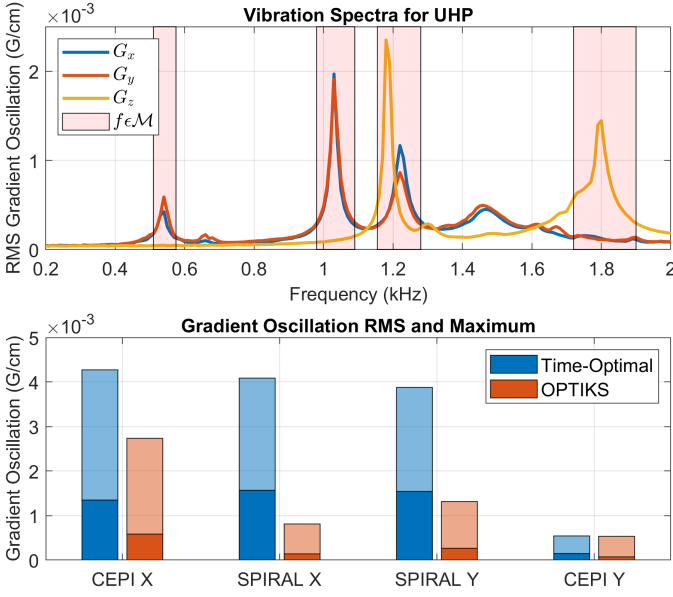


Fig. 4. (TOP) RMS gradient field oscillation spectra for the 3T GE UHP system on X (blue), Y (orange), and Z (yellow) axes. Mechanical resonance bands appear as peaks highlighted in red. (BOTTOM) RMS and maximum gradient field oscillations following time-optimal (blue) and OPTIKS (orange) waveforms played on the UHP system. Darker shorter bar gives RMS value, taller lighter bar gives maximum value.

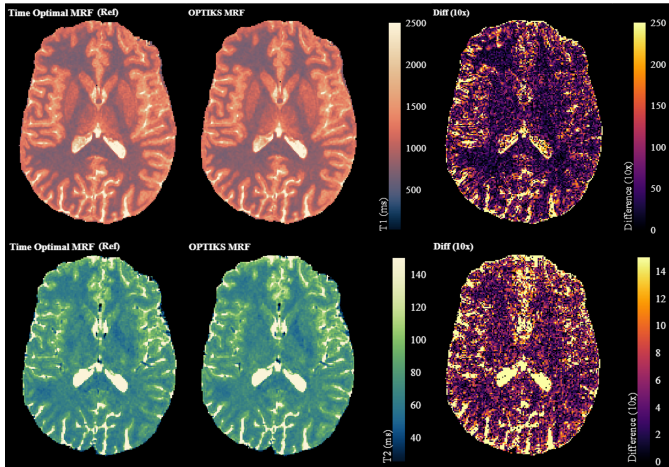


Fig. 5. MRF results using time-optimal spiral and OPTIKS spiral. (TOP) Calculated T1 maps for each acquisition and their 10x difference map. (BOTTOM) Calculated T2 maps for each acquisition and their 10x difference map.

20.6 ms was designed to be time-optimal with slew-rate de-rated to $S_{max} = 8.8$ G/cm/ms. The dBA weighted spectra of each recorded waveform is given in Fig 6. The decrease in peak output for each de-rated and OPTIKS waveform as compared to the time-optimal design is given in Table I. OPTIKS gives a maximum noise decrease of 9.22 dB while the de-rated decreased noise by at most 5.37 dB with the same duration.

IV. DISCUSSION

We have shown that OPTIKS is a powerful tool for optimizing time-domain properties of fast arbitrary trajectory

Quiet Spiral Acoustic Noise Decrease on PREMIER System		
Coil Axis	De-Rated	OPTIKS
X-Axis Decrease (dBA)	4.59 ± 0.02	5.75 ± 0.15
Y-Axis Decrease (dBA)	5.37 ± 0.26	9.22 ± 0.17

TABLE I
PEAK ACOUSTIC NOISE DECREASES FROM DE-RATED AND OPTIKS SPIRALS PLAYED ON PREMIER AS COMPARED TO TIME-OPTIMAL DESIGN.

waveforms. Here we will discuss the trade-offs between OPTIKS and time-optimal waveforms, and interpret the solutions provided by this new design method.

A. Peripheral Nerve Stimulation Performance

OPTIKS was employed to design PNS-limited waveforms which minimize duration subject to S_{max} , G_{max} , and P_{max} constraints. It was shown that the OPTIKS waveforms trade off slew-rate and PNS as limiting regimes in waveform design. The spiral waveform example produces a similar result to [9], where the center of k -space is slew-limited, and slew-rate is decreased when entering the PNS-limited regime. The speed boost for the spiral trajectory in the center of k -space would result in less $T2^*$ decay and lower off resonance phase accumulation reducing subsequent blurring. An example point spread function (PSF) was simulated for each waveform given a typical gray matter $T2^*$ of 50 ms and a bulk off-resonance of 10 Hz (Fig 7). From the full-width-half-max of each PSF we can see that for this example the effective resolution of the time-optimal waveform is 2.82 mm while the OPTIKS waveform maintains a sharper image at 2.09 mm. The rosette trajectory also alternates between slew and PNS-limited regimes with each petal. In both cases the OPTIKS waveform exhibited a significant speed up over the naive slew de-rated waveform while meeting the same P_{max} . The OPTIKS design method improves on [9] by generalizing to arbitrary trajectories without adjustment as demonstrated with the rosette trajectory and rewind MRF spiral.

B. Mechanical Resonance Performance

OPTIKS waveforms were shown to drastically reduce the measured back-EMF and gradient field oscillations implying that mechanical resonance frequencies were avoided. The relative cost in speed was much lower for spiral designs than the CEPI trajectory. This is likely because the smooth spiral designs are easier to optimize without violating slew-rate constraints. Slew-rate in trajectories with regions of high curvature such as in CEPI would be very sensitive to increases in $v(s)$. The phase encode axis of the CEPI waveforms deposits very little power in the mechanical resonance bands without OPTIKS, but is still further reduced during the optimization.

The k -space speed plots in Fig. 3 d) show how $v(s)$ was optimized along the trajectory to avoid resonances. In the case of the spiral the speed is decreased along some radii in a manner similar to the instantaneous frequency assumption of [13]. The improvement here relies on more subtle variation of the speed along the curve to avoid narrow resonance bands and

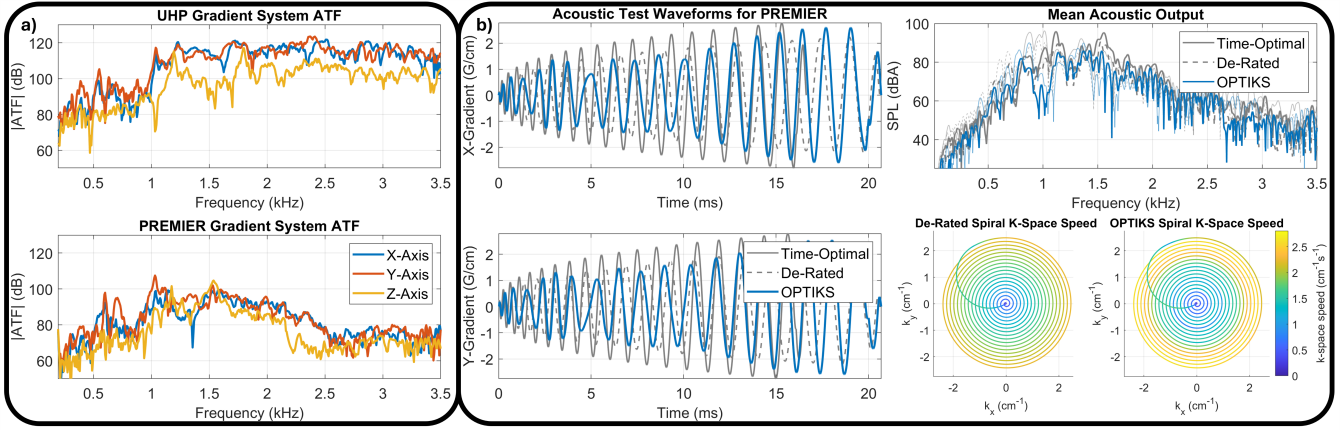


Fig. 6. Acoustic noise reduction experiment. **a)** Measured ARF for UHP and PREMIER gradient systems on X, Y, and Z axes. **b)** Test waveforms and measured outputs. Time-optimal (grey), slew-de-rated (dashed grey), and acoustic optimized OPTIKS X and Y spiral waveforms designed for quiet imaging on PREMIER and measured output on PREMIER. Dark and lighter output lines indicate X and Y axes respectively. K-Space speed plots for de-rated and OPTIKS waveforms on the same colour axis.

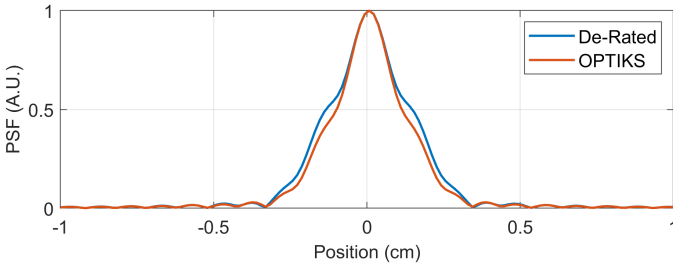


Fig. 7. Point spread functions for slew de-rated and OPTIKS PNS-limited spiral designs. Simulated under T_2^* decay and bulk off-resonance. Cropped to 1 cm radius to illustrate improved sharpness of OPTIKS readout.

transient effects, as well as the ability to include a rewind in the trajectory. The CEPI design varies its speed for each line to avoid switching periods which fall directly into resonance bands or place harmonics in them.

The MRF maps appear qualitatively similar but show an approximate 3% and 5% difference in T1 and T2 respectively for the grey and white matter, with higher differences localized to the cerebral spinal fluid. These differences are within the repeatability margins reported for the 2 minute MRF sequence used [22].

C. Acoustic Noise Performance

It has been shown that ATFs can have high positional dependence [17]. In this work two microphones were used, spaced equally apart from the scanner isocenter. At high frequencies these measurements diverged somewhat, likely due to formation of standing waves within the bore. To address this, the maximum of the two values was taken at each frequency for use in the acoustic noise minimization design (9). Additionally, the microphones used exhibit high directional dependence due to the noise-canceling headphone form-factor. The goal here is to provide a proof of concept for using OPTIKS to design quieter waveforms. The results of the acoustic spiral PREMIER test show a greater decrease in noise from the Y gradient axis than the X. This is likely

due to more dramatic peaks and troughs in the Y axis ATF below 1 kHz, which the OPTIKS method takes advantage of for greater noise reduction. We showed that OPTIKS can outperform a naively de-rated waveform of equal duration by exploiting knowledge of system frequency response to band-limit itself and avoid frequencies of high transference. Further studies could expand upon this by use of an omnidirectional microphone and measurements over an array of positions.

D. Optimality and Convergence

The OPTIKS design functional is not convex and a given solution cannot be called globally optimal. The use of “leaky” log-barrier functions (3) to enforce constraints reducing parameters below the maximum allowed thresholds. A piecewise function with zero slope below the maximum threshold would avoid this issue, but would frequently violate limits during optimization due to the vanishing gradient. There is a trade off then between limit enforcement and operating efficiently close to the limit. This can be adjusted by applying a small coefficient to push the slope towards zero below the threshold, and setting δ small to ensure a large slope beyond the threshold.

V. CONCLUSION

A novel design method for optimization of time-domain gradient properties along arbitrary trajectories was developed, and made available as an open source Python package (<https://github.com/mattmc-stanford/optiks>). The OPTIKS method is highly flexible to customized loss functions, opening up trajectory constrained time-efficient gradient design to a host of new design goals. OPTIKS waveforms were shown to reduce readout time in PNS-limited scans, design quieter spiral waveforms, and avoid gradient mechanical resonances. These waveforms have the potential to increase patient comfort and reduce system strain while maintaining image quality in efficient time.

APPENDIX A

INTERPOLATION BACKWARD PASS

Linear interpolation of a pair of vectors $\mathbf{x}, \mathbf{y} \in \mathbb{R}^{m \times 1}$ to a pair $\mathbf{p}, \mathbf{q} \in \mathbb{R}^{n \times 1}$ consists of binning the independent values \mathbf{p} into \mathbf{x} and averaging the surrounding dependent values from \mathbf{y} based on their distance to the new point. An example is given in (11) where (x_{j-1}, y_{j-1}) and (x_j, y_j) surround the new point (p_i, q_i)

$$q_i = y_{j-1} \left(\frac{x_j - p_i}{x_j - x_{j-1}} \right) + y_j \left(\frac{p_i - x_{j-1}}{x_j - x_{j-1}} \right). \quad (11)$$

We define two permutation matrices $P_1, P_2 \in \mathbb{R}^{n \times m}$ which copy select values in \mathbf{x} and \mathbf{y} such that the surrounding values align with the new points (12) and define a third matrix $P_3 \equiv P_2 - P_1$

$$(P_1 \mathbf{x})_i \leq p_i \leq (P_2 \mathbf{x})_i \quad \forall i = 1, \dots, n. \quad (12)$$

The forward pass of interpolation can then be written using the original and interpolant vectors as in (13)

$$\begin{aligned} \mathbf{q} = & \text{diag}(P_1 \mathbf{y}) \left(\frac{P_2 \mathbf{x} - \mathbf{p}}{P_3 \mathbf{x}} \right) \\ & + \text{diag}(P_2 \mathbf{y}) \left(\frac{\mathbf{p} - P_1 \mathbf{x}}{P_3 \mathbf{x}} \right). \end{aligned} \quad (13)$$

The construction of the sorting matrices is not differentiable and cannot be included in the backpropagation algorithm. However, if we treat them as constant at each gradient descent step, we can approximate the backward pass as in (14)

$$\begin{aligned} \nabla_{\mathbf{x}} \mathbf{q} \approx & \text{diag} \left(\frac{P_1 \mathbf{y}}{P_3 \mathbf{x}} \right) \left[P_2^T - \text{diag} \left(\frac{P_2 \mathbf{x} - \mathbf{p}}{P_3 \mathbf{x}} \right) P_3^T \right] \\ & + \text{diag} \left(\frac{P_2 \mathbf{y}}{P_3 \mathbf{x}} \right) \left[\text{diag} \left(\frac{\mathbf{p} - P_1 \mathbf{x}}{P_3 \mathbf{x}} \right) P_3^T - P_1^T \right] \\ \nabla_{\mathbf{p}} \mathbf{q} \approx & \text{diag} \left(\frac{(P_1 + P_2) \mathbf{y}}{P_3 \mathbf{x}} \right). \end{aligned} \quad (14)$$

REFERENCES

- [1] N. Gudino and S. Littin, "Advancements in gradient system performance for clinical and research MRI," *Journal of Magnetic Resonance Imaging*, vol. 57, no. 1, pp. 57–70, 2023.
- [2] S. A. Winkler, F. Schmitt, H. Landes, J. de Bever, T. Wade, A. Alejski, and B. K. Rutt, "Gradient and shim technologies for ultra high field MRI," *NeuroImage*, vol. 168, pp. 59–70, 2018. Neuroimaging with Ultra-high Field MRI: Present and Future.
- [3] K. F. King, T. K. F. Foo, and C. R. Crawford, "Optimized gradient waveforms for spiral scanning," *Magnetic Resonance in Medicine*, vol. 34, no. 2, pp. 156–160, 1995.
- [4] D.-h. Kim, E. Adalsteinsson, and D. M. Spielman, "Simple analytic variable density spiral design," *Magnetic Resonance in Medicine*, vol. 50, no. 1, pp. 214–219, 2003.
- [5] C. Lazarus, P. Weiss, N. Chauffert, F. Mauconduit, L. El Gueddari, C. Destrieux, I. Zemmoura, A. Vignaud, and P. Ciuciu, "SPARKLING: variable-density k-space filling curves for accelerated T2*-weighted MRI," *Magnetic Resonance in Medicine*, vol. 81, no. 6, pp. 3643–3661, 2019.
- [6] G. Wang, T. Luo, J.-F. Nielsen, D. C. Noll, and J. A. Fessler, "B-spline parameterized joint optimization of reconstruction and k-space trajectories (BJORK) for accelerated 2D MRI," *IEEE Transactions on Medical Imaging*, vol. 41, no. 9, pp. 2318–2330, 2022.
- [7] G. Wang, J.-F. Nielsen, J. A. Fessler, and D. C. Noll, "Stochastic optimization of three-dimensional non-cartesian sampling trajectory," *Magnetic Resonance in Medicine*, vol. 90, no. 2, pp. 417–431, 2023.
- [8] "Medical electrical equipment - part 2–33: particular requirements for the basic safety and essential performance of magnetic resonance equipment for medical diagnosis," standard, International Electrotechnical Commission, Aug. 2022.
- [9] R. F. Schulte and R. Noeske, "Peripheral nerve stimulation-optimal gradient waveform design," *Magnetic Resonance in Medicine*, vol. 74, no. 2, pp. 518–522, 2015.
- [10] N. Boulant, Q. Guihard, O. Dubois, H. Lannou, F.-P. Juster, J. Belorgey, F. Nunio, A. Amadon, C. Bonnelye, V. Gras, C. Le Ster, F. Mauconduit, A. Vignaud, L. Quettier, and G. Aubert, "Measurements of the gradient-induced power deposition in the He-bath of the isult 11.7T magnet and comparison with theory," in *Proceedings of the 32nd Annual Meeting of ISMRM*, (Singapore), p. 3938, 2024.
- [11] J. G. Pipe and D. D. Borup, "Generating spiral gradient waveforms with a compact frequency spectrum," *Magnetic Resonance in Medicine*, vol. 87, no. 2, pp. 791–799, 2022.
- [12] A. T. Curtis, C. K. Anand, C. T. Harris, J. A. Stainsby, and P. J. Beatty, "Method and system of frequency constrained gradient waveform production," 2017.
- [13] M. A. McCready, C. Liao, J. M. Pauly, and A. B. Kerr, "Safe spirals for your scanner," in *Proceedings of the 32nd Annual Meeting of ISMRM*, (Singapore), p. 0946, 2024.
- [14] F. Hennel, F. Girard, and T. Loenneker, "'silent' MRI with soft gradient pulses," *Magnetic Resonance in Medicine*, vol. 42, no. 1, pp. 6–10, 1999.
- [15] Z. Zhou, A. Alfayad, T. C. Chao, and J. G. Pipe, "Acoustic noise reduction for spiral MRI by gradient derating," *Magnetic Resonance in Medicine*, vol. 90, no. 4, pp. 1547–1554, 2023.
- [16] C. V. Rizzo Sierra, M. J. Versluis, J. M. Hoogduin, and H. Duifhuis, "Acoustic fmri noise: Linear time-invariant system model," *IEEE Transactions on Biomedical Engineering*, vol. 55, no. 9, pp. 2115–2123, 2008.
- [17] T. Hamaguchi, T. Miyati, N. Ohno, T. Matsushita, T. Takata, Y. Mat-suura, S. Kobayashi, and T. Gabata, "Spatial analysis of acoustic noise transfer function with a human-body phantom in a clinical MRI scanner," *Acta Radiologica*, vol. 64, no. 3, pp. 1212–1221, 2023. PMID: 35538857.
- [18] M. Lustig, S.-J. Kim, and J. M. Pauly, "A fast method for designing time-optimal gradient waveforms for arbitrary k-space trajectories," *IEEE Transactions on Medical Imaging*, vol. 27, no. 6, pp. 866–873, 2008.
- [19] F. X. Herbank and M. Gebhardt, "SAFE-model - a new method for predicting peripheral nerve stimulations in MRI," in *Proceedings of the 8th Annual Meeting of ISMRM*, (Denver, Colorado, USA), p. 2007, 2000.
- [20] X. Cao, H. Ye, C. Liao, Q. Li, H. He, and J. Zhong, "Fast 3D brain MR fingerprinting based on multi-axis spiral projection trajectory," *Magnetic Resonance in Medicine*, vol. 82, no. 1, pp. 289–301, 2019.
- [21] X. Cao, C. Liao, S. S. Iyer, Z. Wang, Z. Zhou, E. Dai, G. Liberman, Z. Dong, T. Gong, H. He, J. Zhong, B. Bilgic, and K. Setsompop, "Optimized multi-axis spiral projection MR fingerprinting with subspace reconstruction for rapid whole-brain high-isotropic-resolution quantitative imaging," *Magnetic Resonance in Medicine*, vol. 88, no. 1, pp. 133–150, 2022.
- [22] M. Yablonski, Z. Zhou, X. Cao, S. Schauman, C. Liao, K. Setsompop, and J. D. Yeatman, "Fast and reliable quantitative measures of white matter development with magnetic resonance fingerprinting," *Imaging Neuroscience*, vol. 3, p. imag_a_00470, 02 2025.